RSC Advances

PAPER

View Article Online
View Journal | View Issue

Cite this: *RSC Adv.*, 2022, **12**, 31276

Fluorinated covalent organic frameworks for efficient drug delivery†

Baiwei Ma,[a] Yimeng Xu,[a] Fujia Hu,[a] Lipeng Zhai,[*ab] Yongyu Huang,[a] Huijie Qiao,[a] Jiabin Xiong,[a] Dehong Yang,[a] Zhihui Ni,[b] Xiaofei Zheng[*c] and Liwei Mi[*ab]

Received 3rd September 2022
Accepted 27th October 2022

DOI: 10.1039/d2ra05534a

rsc.li/rsc-advances

In this study, two novel fluorine-functionalized crystalline covalent organic frameworks (COFs), namely DF-TAPB-COF and DF-TATB-COF, were synthesized, and their ordered structure, porosity, suitable pore size, and abundant fluorine groups were expected to serve as effective carriers in drug delivery. The excellent cell viability of DF-TAPB-COF and DF-TATB-COF was verified using MTT assays. Both COFs exhibited very high loading capacities in terms of drug loading performance, in particular the drug loading rate of DF-TAPB-COF for 5-fluorouracil (5-FU) was up to 69%. They also exhibited efficient drug release performance in a simulated body fluid environment. Cell endocytosis experiments demonstrated that DF-TAPB-COF and DF-TATB-COF could be effectively endocytosed by cells. Hence, this study offers new insight into the design and development of COF-based drug carrier systems.

Introduction

To date, several drug molecules have not functioned selectively in diseased organs or tissues, because they typically spread throughout the entire body without selectivity, causing various toxic side effect.[1–3] In addition, direct implementation of drugs in patients has some limitations, such as low stability and dispersibility in aqueous solutions, poor penetration into the cell membrane, low targeting efficiency, and unregulated drug delivery.[4,5] Hence, drug carriers, particularly porous nanoparticle materials, which have good drug-loading ability and targeting efficiency, could overcome these limitations.[6–8]

In recent years, covalent organic frameworks (COFs) have become the most popular porous materials because of their unique characteristics, such as low density, excellent crystallinity, porosity, various functionalities, high surface area, adjustable pore size, thermal and chemical stability, and the absence of metals.[9] A variety of COFs have been synthesized and investigated in various applications in recent decades, such as gas storage and separation,[10,11] sensors,[12–15] catalysis,[16,17] energy storage,[18,19] and electrochemical sensing.[20,21] COFs can be applied as drug loading and release systems[22] because of their good stability, large specific surface area, highly porous structures, hypotoxicity and heavy metal-free features. In 2015, Yan *et al.* reported the PI-COF-4 and PI-COF-5 with 20 and 24 wt% loading rates, respectively. And 95% of the initial IBU loading was released after approximately 6 days. This study is the first to apply COF materials in drug delivery.[23] In 2016, Lotsch *et al.* reported an imine-based TTI-COF as a drug delivery vehicle for quercetin transport with 35 wt% loading rate.[24] In the same year, Zhao *et al.* developed PI-3-COF and PI-2-COF with 16 and 30 wt% loading rates for 5-FU, respectively, and the 5-FU drug was completely released by the two COFs after 5 days.[25] In 2017, Banerjee *et al.* developed a TpASH-FA covalent organic nanosheet as a drug delivery material with 12 wt% loading rate for 5-FU.[26] Other studies on COFs as drug delivery systems had also been reported.[27–34]

However, to date, COFs have not been sufficiently studied as drug loading and delivery candidates, and the ability of COF materials to load drugs still need to be improved significantly. As shown in Table S1,† the drug loading rates of various synthesized COFs had been typically found to be 10–40 wt%. Hence, there is an urgent need to explore novel COF platforms for efficient targeted drug release.

Here, two new fluorine-functionalized imine-linked COFs, DF-TAPB-COF and DF-TATB-COF, were designed and synthesized *via* the condensation reaction of 2,5-difluoro terephthalaldehyde (DFPA) with 1,3,5-tri-(4-aminophenyl) benzene (TAPB) or 4,4′,4″-(1,3,5-triazine-2,4,6-triyl)trianiline (TATB) under solvothermal conditions (Fig. 1). In order to prove the potential capacity of the two COFs in drug delivery, 5-FU with anti-tumor activity and captopril (CA) with antihypertensive ability were chosen as research objects. The structures of 5-FU and CA drug contain amide, carboxyl and sulfydryl groups, respectively. These groups could form F–H hydrogen bonds

[a]School of Material and Chemical Engineering, Zhongyuan University of Technology, Zhengzhou, 450007 P. R. China. E-mail: zhailp@zut.edu.cn

[b]Henan Key Laboratory of Functional Salt Materials, Center for Advanced Materials Research, Zhongyuan University of Technology, Zhengzhou, 450007 P. R. China. E-mail: mlwzzu@163.com

[c]Department of Stomatology, The First Affiliated Hospital of Zhengzhou University, Zhengzhou, 450052 P. R. China. E-mail: zheng-xiaofei2008@163.com

† Electronic supplementary information (ESI) available. See DOI: https://doi.org/10.1039/d2ra05534a

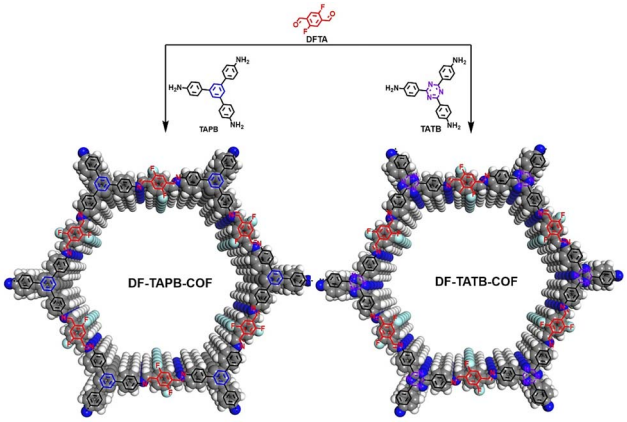

Fig. 1 Schematic representation of synthesis of DF-TAPB-COF and DF-TATB-COF (H, white; C, gray; N, blue; F, cyan).

with fluorine groups of the COFs, which make the two drugs more easily loaded into the COFs. In addition, the two COFs with large pore canals could accommodate more drug molecules *via* noncovalent bond forces. And these two COFs can be used as carriers to achieve better water dispersion by introducing a more hydrophilic fluorine group. Hence, the two well-designed COFs could be as promising candidates for drug delivery systems.

Experimental

Characterization

Solid state Fourier ^{13}C NMR spectra were measured on a Bruker 400 MHz spectrometer. Transform infrared (FT IR) spectra were recorded on a JASCO model FT IR-6100 infrared spectrometer. X-ray diffraction (XRD) data were recorded on a Bruker D8 Focus Powder X-ray Diffractometer by using powder on glass substrate, from $2\theta = 2°$ up to 30° with 0.5° increment. TGA measurements were performed on a Discovery TGA under N_2, by heating from 30 °C to 800 °C at a rate of 10 °C min^{-1}. Nitrogen sorption isotherms were measured at 77 K with a TriStar II instrument (Micromeritics). The Brunauer–Emmett–Teller (BET) method was utilized to calculate the specific surface areas. By using the non-local density functional theory (NLDFT) model, the pore volume was derived from the sorption curve. Morphology images were characterized with a Zeiss Merlin Compact filed emission scanning electron microscope (FE-SEM) equipped with an energy-dispersive X-ray spectroscopy (EDS) system at an electric voltage of 5 KV. UV-vis spectra were recorded on a PerkinElmer Lambda 950 UV/VIS/NIR spectrometer.

Synthesis of DF-TAPB-COF

A Pyrex tube (10 ml) is charged with 1,3,5-tri-(4-aminophenyl) benzene (TAPB) (0.08 mmol), 2,5-difluoroterephthalaldehyde (DFPA) (0.16 mmol), 0.5 mL *o*-DCB, 0.5 mL 1-butanol and 0.1 mL of 6 M aqueous acetic acid. The tube was then flash frozen at 77 K and degassed by three freeze-pump-thaw cycles. The tube was sealed off and then heated at 120 °C for 3 days. The collected powder was washed with dimethylformamide and tetrahydrofuran, then dried at 80 °C under vacuum for 24 hours to get corresponding yellow powder in ~89% isolated yield.

Synthesis of DF-TATB-COF

A Pyrex tube (10 ml) is charged with 4,4′,4″-(1,3,5-triazine-2,4,6-triyl)trianiline (TATB) (0.08 mmol), 2,5-difluoroterephthalaldehyde (DFPA) (0.16 mmol), 0.5 mL mesitylene, 0.5 mL dioxane and 0.1 mL of 6 M aqueous acetic acid. The tube was then flash frozen at 77 K and degassed by three freeze-pump-thaw cycles. The tube was sealed off and then heated at 120 °C for 3 days. The collected powder was washed with dimethylformamide and tetrahydrofuran, then dried at 80 °C under vacuum for 24 hours to get corresponding red powder in ~85% isolated yield.

Result and discussion

Structure and description

FT-IR spectroscopy was first used to describe the structure of the synthesized COFs (Fig. 2a and b). The characteristic stretching peaks at 1490 and 1511 cm^{-1} indicate the formation of C=N bonds at the joints of DF-TAPB-COF and DF-TATB-COF, respectively.

^{13}C SS-NMR spectroscopy was used to describe the structures of DF-TAPB-COF and DF-TATB-COF (Fig. 3). The carbon signal for the C=N and C–F groups on the aromatic ring of DF-TAPB-

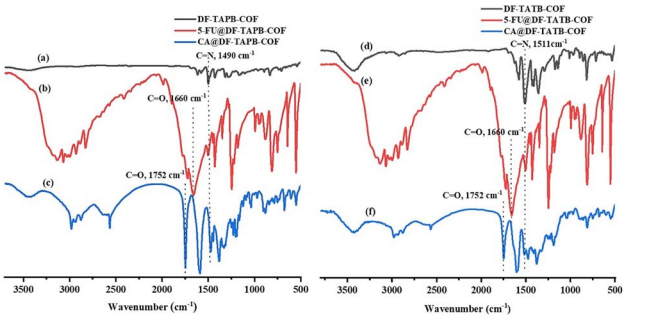

Fig. 2 FT-IR spectrum of DF-TAPB-COF ((a) black), 5-FU@DF-TAPB-COF ((b) red), CA@DF-TAPB-COF ((c) blue), DF-TATB-COF ((d) black), 5-FU@DF-TATPB-COF ((e) red) and CA@DF-TATB-COF ((f) blue).

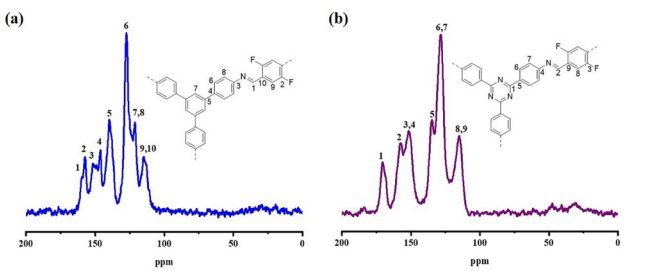

Fig. 3 Solid state ^{13}C CP-MAS NMR spectrum patterns of DF-TAPB-COF (a) and DF-TATB-COF (b).

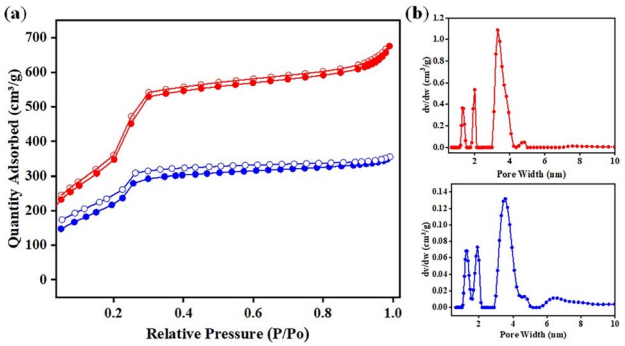

Fig. 4 (a) Nitrogen sorption isotherms at 77 K of (red) DF-TAPB-COF and (blue) DF-TATB-COF; (b) pore size distributions of (red) DF-TAPB-COF and (blue) DF-TATB-COF calculated using non-local density functional theory.

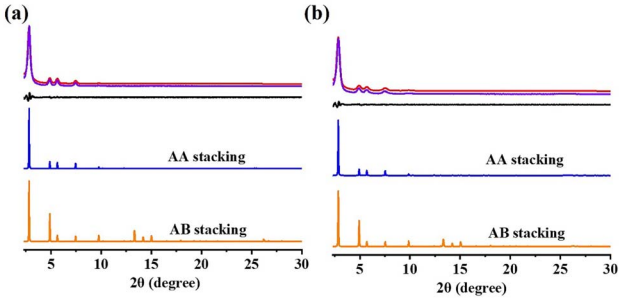

Fig. 5 PXRD patterns of (a) DF-TAPB-COF and (b) DF-TATB-COF: experimental (red), Pawley refined PXRD patterns (purple), corresponding difference (black), the simulated patterns for eclipsed AA stacking mode (blue) and the staggered (AB) layer stacking mode (orange).

COF appeared at 159.6 and 157.4 ppm, respectively, whereas the carbons of benzene rings appeared at 151.9–112.8 ppm. For DF-TATB-COF, the C=N peaks of the triazine rings were detected at 170.8 ppm. The peaks of C=N at the joint of DF-TATB-COF and C–F groups on the aromatic ring appeared at 157.4 and 152.2 ppm, respectively, whereas the carbon signals of the benzene rings appeared at 152.4–114.5 ppm.

Nitrogen adsorption–desorption isotherms at 77 K were used to determine the porous characteristics of DF-TAPB-COF and DF-TATB-COF. The type-IV adsorption isotherms in Fig. 4a show that the two COFs possess mesopores. The BET surface areas of DF-TAPB-COF and DF-TATB-COF were 1720 and 963 $m^2\ g^{-1}$, respectively. The pore size and distribution were investigated using a nonlocal density functional theory (NLDFT) cylindrical pore model. Two remarkable peaks of DF-TAPB-COF and DF-TATB-COF were found at 3.34 and 3.53 nm, respectively, in the pore size distribution profile of the two COFs (Fig. 4b). The numerical value is similar to the theoretical values calculated for AA layer stacking. For each COF, the corresponding total pore volume was 1.05 and 0.55 $cm^3\ g^{-1}$, respectively.

The morphologies of both COFs were observed using FE-SEM. DF-TAPB-COF exhibited a sphere-like microstructure, whereas that of DF-TATB-COF was granular (Fig. S1†). Energy-dispersive X-ray (EDX) spectroscopy mapping of the COFs exhibited a uniform elemental dispersion in their structural networks (Fig. S2†).

The crystalline structures of these COFs were resolved using powder XRD (PXRD). PXRD analysis (Fig. 5) was used to describe the crystallinity of the DF-TAPB-COF and DF-TATB-COF. The PXRD pattern of DF-TAPB-COF exhibited characteristic diffraction peaks at 2.84°, 4.86°, 5.62°, 7.44°, 9.76°, and 25.36°, which were assigned to the 100, 110, 200, 210, 220, and 001 facets, respectively (Fig. 5a, red curve). The PXRD pattern of DF-TATB-COF exhibited characteristic diffraction peaks at 2.85°, 4.90°, 5.69°, 7.46°, 9.79°, and 25.50°, which were assigned to the 100, 110, 200, 210, 220, and 001 facets, respectively (Fig. 5b, red curve). The self-consistent charge density functional tight binding (SCC-DFTB) method was used for the theoretical analysis of the structure of the two COFs. The Pawley refined XRD patterns (Fig. 5, purple curve) correlated with the experimentally observed pattern, which demonstrated their negligible difference (black curve). The blue curves in Fig. 4 show that the experimental PXRD peak positions and their relative intensities were closer to the patterns of the eclipsed AA stacked structure. By contrast, there were clear deviations between the experimental and simulated patterns of the staggered AB stacked structure (orange curve). Therefore, both COFs adopted AA stacking rather than AB stacking.

Stability

The thermal stabilities of both COFs were examined using TGA. The DF-TAPB-COF was stable up to 400 °C under N_2, and the DF-TATB-COF had negligible loss below 300 °C (Fig. S3†).

The chemical stabilities of the two COFs were examined by dispersing them in a strong acid and base for 48 h, after which their PXRD profiles were assessed after vacuum drying at 80 °C for 48 h. As shown in Fig. S4,† no significant changes in the PXRD peak position and intensity of the COFs were observed after treatment with 1 M HCl and 1 M NaOH for 48 h, indicating that the COFs had excellent chemical stability.

Drug loading capacity of DF-TAPB-COF and DF-TATB-COF

The successful drug loading for the two COFs was explained using PXRD, FT-IR, and TGA analyses. PXRD analysis was used to evaluate the drug-loading properties of the COFs. The characteristic diffraction peaks of DF-TAPB-COF and DF-TATB-COF loaded with 5-FU and CA are shown in Fig. S5.† Not only the diffraction peaks of the two COFs were present, but also the diffraction peaks of 5-FU and CA were observed, indicating that 5-FU and CA were successfully loaded by these two COFs.

Furthermore, the successful loading of 5-FU and CA drugs within the COFs was examined by FT-IR analysis with the explanation of the characteristic peaks from the 5-FU@DF-TAPB-COF, CA@DF-TAPB-COF, 5-FU@DF-TATB-COF, and CA@DF-TATB-COF in comparison with the two COFs without loaded drugs (Fig. 2a–f). The FT-IR spectra of DF-TAPB-COF, 5-FU@DF-TAPB-COF, and CA@DF-TAPB-COF are shown in Fig. 2a–c, and their C=N stretching vibration peaks were observed at 1490 cm^{-1}, indicating that the structure of the COF

was still maintained after loading 5-FU and CA. The C=O stretching vibration peaks of 5-FU and CA were observed at 1660 cm^{-1} and 1752 cm^{-1} in the 5-FU@DF-TAPB-COF and CA of CA@DF-TAPB-COF, respectively, indicating that these two drugs were successfully loaded by DF-TAPB-COF. In addition, the FT-IR spectra of DF-TATB-COF, 5-FU@DF-TATB-COF, and CA@DF-TATB-COF are shown in Fig. 2d–f, and their C=N stretching vibration peaks were observed at 1511 cm^{-1}, indicating that the structure of DF-TATB-COF was still stable after encapsulating 5-FU and CA. The C=O stretching vibration peaks of 5-FU and CA were also observed at 1660 and 1752 cm^{-1} in the 5-FU@DF-TATB-COF and CA@DF-TATB-COF, respectively, indicating that these two drugs were successfully loaded by the DF-TATB-COF.

The loading capacities of DF-TAPB-COF and DF-TATB-COF for 5-FU and CA were investigated using TGA. It is evident from the TGA thermogram that 5-FU and CA began to decompose at 253 and 195 °C, respectively (Fig. S6†). Hence, as shown in Fig. S7,† the loading capacities of DF-TAPB-COF and DF-TATB-COF for 5-FU were 69 and 67 wt%, respectively, which are the highest among the reported COF materials. The loading capacity of DF-TAPB-COF for CA was also high (up to 60 wt%). However, the 41 wt% loading capacity of the DF-TATB-COF for CA was lower than that of DF-TAPB-COF, it is because that DF-TATB-COF has a lower BET surface area and pore volume than DF-TAPB-COF. The DF-TATB-COF with more lower BET surface area has less active load sites, and more smaller pore volume of the COF means more weaker ability of accommodating drug molecules into the hole. To prove the importance of fluorine groups for the loading drug capacity of the COFs, we prepared the N-TAPB-OMeTA COF material according to the literature,[35] and its chemical structure and PXRD are shown in Fig. S8.† It can be observed from the TGA thermogram of N-TAPB-OMeTA that it is stable below 350 °C (Fig. S9†). As shown in Fig. S10a and b,† the loading capacity of N-TAPB-OMeTA for 5-FU and CA were 31 and 20 wt%, respectively, which is significantly less than that of our designed DF-TAPB-COF and DF-TATB-COF. This experimental result proved that methoxy groups of the COFs have no intermolecular interation with 5-FU and CA, however, our designed COFs have good loading capacity for 5-FU and CA because of the existence of fluorine groups, which can form F–H hydrogen bonding forces with the two drug molecules. Hence, the introduction of fluorine groups is necessary to improve the loading capacity of the COFs.

In vitro releasing of drugs

The cumulative drug release rate from the drug carrier system was investigated. A linear relationship between the fluorescence intensity and the 5-FU and CA drug concentrations was observed (Fig. S11†), and the 5-FU and CA concentrations ranged from 14 to 70 mg L^{-1} and 20 to 40 mg L^{-1}, respectively. The calibration curves for 5-FU and CA are shown in Fig. S11.†

As shown in Fig. 6, the release behaviors of 5-FU@DF-TAPB-COF, 5-FU@DF-TATB-COF, CA@DF-TAPB-COF, and CA@DF-TATB-COF were investigated in PBS water solution with a pH of 7.4 at 37 °C, respectively. The real-time drug release behavior

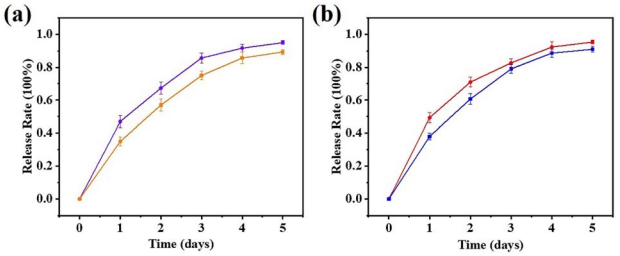

Fig. 6 Release profiles of 5-FU@DF-TAPB-COF ((a) red), 5-FU@DF-TATB-COF ((a) blue), CA@DF-TAPB-COF ((b) purple) and CA@DF-TATB-COF ((b) orange). Data were presented as the mean ± SD ($n = 3$).

was detected by UV-visible spectroscopy based on the calibration curve of 5-FU. The drug release rates of the two 5-FU loaded COFs were similar, and most of the loaded 5-FU was released by 5-FU@DF-TAPB-COF and 5-FU@DF-TATB-COF after 3 d. The cumulative release rate of 5-FU@DF-TAPB-COF was up to 80% of the original loaded 5-FU after 3 d, which was higher than that of 5-FU@DF-TATB-COF. It could be explained by the fact that DF-TAPB-COF with a larger pore volume can release 5-FU more easily than DF-TATB-COF. Furthermore, the two COFs loaded with CA exhibited excellently *in vitro* drug release, which were similar to that of 5-FU loaded COFs. Thus, the synthesized porous COF nanoparticles could serve as suitable materials for drug carriers and release systems.

In vitro cell cytotoxicity

To evaluate the biocompatibility of 5-FU, CA, DF-TAPB-COF, DF-TATB-COF, 5-FU@DF-TAPB-COF, and 5-FU@DF-TATB-COF, an MTT assay was performed using MCF-7 cells. Fig. 7a shows the cell viability after incubation with pure and drug-loaded COFs for 48 h. No significant cytotoxicity was observed at low concentrations (50 μg mL^{-1}) for pure DF-TAPB-COF or DF-TATB-COF. Even when the concentrations of DF-TAPB-COF and DF-TATB-COF were up to 200 μg mL^{-1}, the cytotoxicity of DF-TAPB-COF was still low, resulting in a 96% cell viability. However, a cell viability of 84% was observed for DF-TATB-COF, and there was a certain degree of reduction compared with the low concentration of 50 μg mL^{-1}. Hence, the two COFs exhibited good biocompatibility. The cytotoxic effect of 5-FU and CA at

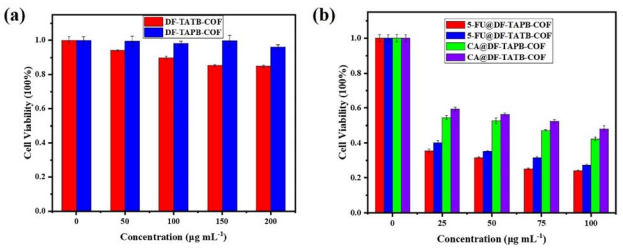

Fig. 7 (a) *In vitro* cell cytotoxicity of DF-TAPB-COF and DF-TATB-COF at 37 °C for 48 h and their concentration scope was at 50–200 μg mL^{-1}; (b) *in vitro* cell cytotoxicity of 5-FU and captopril drug loaded the two COFs at 25–100 μg mL^{-1} for 48 h. Data were presented as the mean ± SD ($n = 3$).

25–100 μg mL^{-1} on MCF-7 cells after incubation for 48 h are shown in Fig. S12.† In addition, the cytotoxic effect of 5-FU and CA loaded COFs at concentrations of 25–100 μg mL^{-1} on MCF-7 cells after incubation for 48 h are shown in Fig. 7b. Interestingly, 5-FU@DF-TAPB-COF and 5-FU@DF-TATB-COF exhibited a higher inhibition rate for cells than pure 5-FU. CA@DF-TAPB-COF and CA@DF-TATB-COF exhibited a slightly higher inhibition rate for cells than pure CA.

Cell uptake of COFs *in vitro*

An inverted fluorescence microscope was used to monitor whether DF-TAPB-COF and DF-TATB-COF could be endocytosed by B16F10 cells (Fig. S13†). Using rhodamine B as the fluorescent labeling reagent, which was loaded into DF-TAPB-COF and DF-TATB-COF, the endocytosis process was performed in B16F10 cells for 6 h at 37 °C. Compared with untreated cells, the fluorescence microscope images of rhodamine B@DF-TAPB-COF and rhodamine B@DF-TATB-COF clearly showed that after 6 h of incubation, they could enter the cytoplasm of B16F10 cells. These results clearly indicated that DF-TAPB-COF and DF-TATB-COF were endocytosed by cells, and thus they could serve as drug carrier systems.[36]

Conclusions

In summary, two novel chemically and thermally stable fluorine-based COFs, namely DF-TAPB-COF and DF-TATB-COF with imine linkages were successfully synthesized and used as drug carrier systems for 5-FU and CA. The two COFs with large mesoporous pores could accommodate abundant drug molecules *via* noncovalent bond forces. In addition, by introducing a more hydrophilic fluorine group, these two COFs can be used as carriers to achieve better water dispersion, and the fluorine groups can improve the drug-loading capacity by forming F–H hydrogen bonding forces with the drug molecules. Hence, these two COFs exhibited high loading capacities and efficient drug release behaviors. MTT assays proved that they possess low cytotoxicity, thus can serve as candidates for biomedical applications. Cell endocytosis experiments demonstrated that DF-TAPB-COF and DF-TATB-COF can be effectively endocytosed by cells, providing a direct proof that they can act as drug carriers. These results indicated that DF-TAPB-COF and DF-TATB-COF could be used as potential drug delivery platforms for cancer or cardiovascular disease chemotherapy. The results of this study can contribute to the development of excellent drug delivery systems.

Author contributions

Baiwei Ma: experiment implementation and guidance, data collection and writing. Yimeng Xu, Fujia Hu, Yongyu Huang, Huijie Qiao, Jiabin Xiong, Dehong Yang and Zhihui Ni: experiment implementation and discussion. Lipeng Zhai: calculations, writing polish and funding support. Xiaofei Zheng: writing polish and funding support. Liwei Mi: project administration and funding support.

Conflicts of interest

There are no conflicts to declare.

Acknowledgements

This work was supported by the National Natural Science Funds of China (Grants U1804126, 21671205, 52103277, 82101052 and 21901264), the Zhongyuan University of Technology Start-up Grant, the Natural Science Foundation of Zhongyuan University of Technology (K2022QN008), the Medical Science and Technology Youth Project of Henan Province (SBGJ202003039), the Health Commission Joint Project of Henan Province (LHGJ20200291) and Key Projects of Science and Technology of Henan Province (No. 212102210208 and 212102210442).

Notes and references

1 M. K.-P. Kusch, W. E. Haefeli and H. M. Seidling, *Patient Educ. Couns.*, 2021, **104**, 2351–2357.
2 S. Pradhan, A. Mishra, S. Sahoo, S. Pradhan, P. J. Babu, Y. D. Singh and N. B. Chanu, *Pharmacol. Res. – Mod. Chin. Med.*, 2022, **2**, 100064.
3 V. P. Torchilin, *Eur. J. Pharm. Sci.*, 2000, **11**, S81–S91.
4 Z. Liu, K. Chen, C. Davis, S. Sherlock, Q. Cao, X. Chen and H. Dai, *Cancer Res.*, 2008, **68**, 6652–6660.
5 J. Zhuang, C. H. Kuo, L. Y. Chou, D. Y. Liu, E. Weerapana and C. K. Tsung, *ACS Nano*, 2014, **8**, 2812–2819.
6 G. Hong, S. Diao, A. L. Antaris and H. Dai, *Chem. Rev.*, 2015, **115**, 10816–10906.
7 G. Y. Zhang, X. L. Li, Q. B. Liao, Y. F. Liu, K. Xi, W. Y. Huang and X. D. Jia, *Nat. Commun.*, 2018, **9**, 2785.
8 M. Arruebo, *Wiley Interdiscip. Rev.: Nanomed. Nanobiotechnology*, 2012, **4**, 16–30.
9 R. Y. Ke, T. Tan, Y. F. Gong, Y. Z. Chen, Z. E. Li, S. L. Xie, T. He, Z. Lu, H. Yang and D. L. Jiang, *Chem. Soc. Rev.*, 2021, **50**, 120–242.
10 J. Li, X. Zhou, J. Wang and X. F. Li, *Ind. Eng. Chem. Res.*, 2019, **58**, 15394–15406.
11 D. Cui, X. S. Ding, W. Xie, G. J. Xu, Z. M. Su, Y. H. Xu and Y. Z. Xie, *CrystEngComm*, 2021, **23**, 5569–5574.
12 T. Skorjanc, D. Shetty and M. Valant, *ACS Sens.*, 2021, **6**, 1461–1481.
13 F. Niu, Z. W. Shao, J. L. Zhu, L. M. Tao and Y. Ding, *J. Mater. Chem. C*, 2021, **9**, 8562–8569.
14 Q. Q. Zhu, H. K. Li, X. L. Sun, Z. Y. Han, J. C. Sun and H. M. He, *J. Mater. Chem. C*, 2021, **9**, 8043–8050.
15 W. R. Cui, C. R. Zhang, W. Jiang, R. P. Liang and J. D. Qiu, *ACS Appl. Nano Mater.*, 2019, **2**, 5342–5349.
16 M. H. Chen, J. B. Zhang, C. X. Liu, H. R. Li, H. W. Yang, Y. Q. Feng and B. Zhang, *Org. Lett.*, 2021, **23**, 1748–1752.
17 H. J. Peng, J. Raya, F. Richard, W. Baaziz, O. Ersen, A. Ciesielski and P. Samor, *Angew. Chem., Int. Ed.*, 2020, **59**, 19602–19609.
18 Z. F. Yang, J. J. Liu, Y. S. Li, G. Zhang, G. L. Xing and L. Chen, *Angew. Chem., Int. Ed.*, 2021, **60**, 20754–20759.

19 M. K. Shehab, K. S. Weeraratne, T. Huang, K. U. Lao and H. M. El-Kaderi, *ACS Appl. Mater. Interfaces*, 2021, **13**, 15083–15091.
20 J. H. Liu, W. H. Zhou, R. Z. Zhao, Z. D. Yang, W. Li, D. L. Chao, S. Z. Qiao and D. Y. Zhao, *J. Am. Chem. Soc.*, 2021, **143**, 15475–15489.
21 L. Y. Wang, Y. Xie, Y. X. Yang, H. H. Liang, L. Wang and Y. H. Song, *ACS Appl. Nano Mater.*, 2020, **3**, 1412–1419.
22 M. C. Scicluna and L. Vella-Zarb, *ACS Appl. Nano Mater.*, 2020, **3**, 3097–3115.
23 Q. R. Fang, J. H. Wang, S. Gu, R. B. Kaspar, Z. B. Zhuang, J. Zheng, H. X. Guo, S. L. Qiu and Y. S. Yan, *J. Am. Chem. Soc.*, 2015, **137**, 8352–8355.
24 V. S. Vyas, M. Vishwakarma, I. Moudrakovski, F. Haase, G. Savasci, C. Ochsenfeld, J. P. Spatz and B. V. Lotsch, *Adv. Mater.*, 2016, **28**, 8749–8754.
25 L. Bai, S. Z. F. Phua, W. Q. Lim, A. Jana, Z. Luo, H. P. Tham, L. Zhao, Q. Gao and Y. Zhao, *Chem. Commun.*, 2016, **52**, 4128–4131.
26 S. Mitra, H. S. Sasmal, T. Kundu, S. Kandambeth, K. Illath, D. D. Díaz and R. Banerjee, *J. Am. Chem. Soc.*, 2017, **139**, 4513–4520.
27 L. Akyuz, *Microporous Mesoporous Mater.*, 2020, **294**, 109850.
28 Y. T. Jia, L. N. Zhang, B. N. He, Y. L. Lin and J. W. Meng, *Mater. Sci. Eng., C*, 2022, **117**, 111243.
29 M. Li, Y. Peng, F. Yan, C. G. Li, Y. Q. He, Y. Lou, D. X. Ma, Y. Li, Z. Shi and S. H. Feng, *New J. Chem.*, 2021, **45**, 3343–3348.
30 G. Y. Zhang, X. L. Li, Q. B. Liao, Y. F. Liu, K. Xi, W. Y. Huang and X. D. Jia, *Nat. Commun.*, 2018, **9**, 2785.
31 K. Zhao, P. W. Gong, J. Huang, Y. Huang, D. D. Wang, J. Y. Peng, D. Y. Shen, X. F. Zheng, J. M. You and Z. Liu, *Microporous Mesoporous Mater.*, 2021, **311**, 110713.
32 A. Ghahari, H. Raissi and F. Farzad, *J. Taiwan Inst. Chem. Eng.*, 2021, **125**, 15–22.
33 R. Anbazhagan, R. Krishnamoorthi, S. Kumaresan and H. C. Tsai, *Mater. Sci. Eng., C*, 2021, **120**, 111704.
34 S. N. Liu, C. L. Hu, Y. Liu, X. Y. Zhao, M. L. Pang and J. Lin, *Chem.–Eur. J.*, 2021, **25**, 4315–4319.
35 C. J. Kang, Z. Q. Zhang, A. K. Usadi, D. C. Calabro, L. S. Baugh, K. Yu, Y. X. Wang and D. Zhao, *J. Am. Chem. Soc.*, 2022, **144**, 3192–3199.
36 X. He, K. Cai, Y. Zhang, Y. Lu, Q. Guo, Y. Zhang, L. Liu, C. Ruan, Q. Chen, X. Chen, C. Li, T. Sun, J. Cheng and C. Jiang, *ACS Appl. Mater. Interfaces*, 2018, **10**, 39455–39467.